Ionic Selective Occupation, Lattice Modulation and Photoluminescence Properties of Garnet Typed Orange-Yellow Phosphors for White-Light-Emitting Diodes

Chen Yang[1], Xinhua Chen[1], Minmin Mao[1, *], Xinjiang Luo[1], Weiqin Sheng[1], Zhilun Lu[2], Shikuan Sun[3], Hong He[4, *], Weitao Su[5], Kaixin Song[1, *]

[1] College of Electronics Information, Hangzhou Dianzi University, Hangzhou, 310018, China

[2] School of Engineering and the Built Environment, Edinburgh Napier University, Edinburgh EH10 5DT, UK

[3] School of Material Science and Energy Engineering, Foshan University, Foshan 528000, China

[4] Department of Science and Technology, Hangzhou Dianzi University, Hangzhou, 310018, China

[5] School of Sciences, Hangzhou Dianzi University, Hangzhou, 310018, China

ABSTRACT

Orange-yellow luminescent $Y_{2-x}Sr_{1-y}Al_4SiO_{12}$: xCe^{3+}, yMn^{2+} (x=0.04-0.06, y=0.1-0.6, abbreviated as YSAS: xCe^{3+}, yMn^{2+}) phosphors with garnet structure were prepared by the high temperature solid-phase method. The matrix energy band is calculated by DFT, where YAG is 4.535 *e*V and YSAS is 4.874 *e*V. The Rietveld

* Corresponding authors: kxsong@hdu.edu.cn;hehong@hdu.edu.cn;mmm@hdu.edu.cn

refinement of the XRD data indicates that Ce^{3+} mainly replaces the Y^{3+} sites, while Mn^{2+} selectively occupies. The Gaussian peaks of the fluorescence spectrum prove that Mn^{2+} occupies two luminescent centers, which are further determined by Van Uitert's empirical formula. The doping of Ce^{3+}/Mn^{2+} units can effectively enhance the structural rigidity of the YAG host and promote the red-shift of the emission peak position of Mn^{2+}. The fluorescence decay kinetics test proves that Ce^{3+} can transfer energy to Mn^{2+}, and the transfer efficiency reaches 72.08% at y=0.5. The thermal stability test of the phosphor shows the luminous intensity at 473K still maintains 86% of the room temperature. The phosphor prepared in this experiment was combined with a blue light chip to make a w-LED device, and the performance showed Ra=86.1, CCT=5168K. The above results show that the emission color of the garnet structure can be tuned by energy transfer, which is attractive for future applications.

Keywords: garnet structure; phosphors; luminescent; w-LED device;

1. Introduction

There are numerous strategies to improve the color rendering and performance of white light illumination, including polymers, small molecule organic and inorganic light-emitting diodes, etc. [1,2], but the most prevalent used strategy is the down-conversion strategy of coating phosphors on UV/blue LED chips [3]. Phosphor-based white light lighting devices offer numerous benefits, such as environmental protection, high efficiency, and tunable light emission [4,5]. At present, YAG: Ce^{3+} series phosphors are the most mainstream commercial phosphors in the market [6]. However,

white LEDs made with such phosphors still suffer from some disadvantages due to the lack of red components, such as low color rendering index and high color temperature, which hinder their application in high-quality white light [7,8]. Researchers have discovered multiple red phosphors with excellent luminescence properties, such as: K_2SiF_6: Mn^{4+} [9], $Sr_2Si_5N_8$: Eu^{2+} [10] and Y_2O_2S: Eu^{3+} [11], etc. However, However, the majority of these phosphors are generated under harsh conditions, and some even pollute the environment. Therefore, controlling the structure of YAG: Ce^{3+} and increasing its red-light component is of crucial practical importance.

Under this research context, many researchers have carried out extensive research on the structural regulation of YAG: Ce^{3+}. Tong [12] et al. prepared a series of $Y_3MgAl_3SiO_{12}$: Ce^{3+}, Mn^{2+} phosphors in the author's group. Among them, Ce^{3+} occupied the lattice position of Y^{3+}, Mn^{2+} occupied two lattice positions of Mg-O_6 octahedron and Al-O_4 tetrahedron, respectively emitting orange light at 613 nm (Mn^{2+}(I)) and 723 nm (Mn^{2+}(II)). Using this phosphor coupled with a blue chip to fabricate a w-LED, and its performance was CRI=85.4, CCT=4502 K, which has potential application value. Jia [13] et al. used Mn^{2+}-Si^{4+} units to replace Y^{3+}-Al^{3+} units in the YAG structure for structural control, it was found that Mn^{2+} replaces Y^{3+} and Si^{4+} replaces Al^{3+} to conserve charge and the prepared YAG: Ce^{3+}, Mn^{2+}, Si^{4+} phosphors exhibited yellow emission of Ce^{3+} and red emission of Mn^{2+}. Through the energy transfer from Ce^{3+} to Mn^{2+}, the chromaticity coordinates are transformed from (0.425, 0.550) to (0.502, 0.482), which makes up for the insufficient red-light

component in the YAG: Ce^{3+} phosphor. Ji [14] et al. used Ba^{2+}-Si^{4+} units to replace Y^{3+}-Al^{3+} units in the YAG: Ce^{3+}, resulting in yellow emission at 460 nm excitation with a peak around 537 nm, and the luminescence intensity at 200°C still retains 91.5% of that at room temperature, which is due to the high crystallinity of the crystals. Meng [15] et al. prepared a series of $[(Gd_{0.6}Lu_{0.4})_{1-y}Ce_y]_3[Al_{1-z}(Mg/Si)_z]_5O_{12}$ phosphors by gel synthesis method and studied the effect of Mg^{2+}-Si^{4+} unit substitution on the host structure of garnet. The results showed that the co-doping of Mg^{2+}-Si^{4+} units narrowed the forbidden band width of the matrix, the Ce-O_8 dodecahedron was not uniformly compressed, and the Al-O polyhedron expanded. The alteration of the polyhedral structure within the matrix reduces the luminescence intensity, fluorescence lifetime and thermal stability of Ce^{3+}, but promotes the red-shift of the peak position of the emission spectrum. According to the aforementioned reports, the structural modulation of YAG may expand the range of emission spectrum, but the performance and luminous intensity of phosphors still need to be further improved.

In $Y_3Al_5O_{12}$ garnet, Y^{3+} ionic site combines with eight oxygen atoms to form a Y-O_8 dodecahedron structure (Fig. S1 Y-O_8 dodecahedron). Al^{3+} has two sets of ionic sites of Al(1) and Al(2). Al(1) combines with six oxygen atoms to form Al_1-O_6 octahedron (Fig. S1 Al_1-O_6 octahedron), and Al(2) combines with four oxygen atoms to form Al_2-O_4 tetrahedral structure (Fig. S1 Al_2-O_4 tetrahedron). Each Al_2-O_4 tetrahedron is connected to four Al_1-O_6 octahedra, and each Al_1-O_6 octahedron is connected to six Al_1-O_4 tetrahedra. In this paper, Sr^{2+}-Si^{4+} units are designed to replace Y^{3+}-Al^{3+} units in $Y_3Al_5O_{12}$ (YAG) to form $Y_2SrAl_4SiO_{12}$ (YASA), a derivative

structure of YAG. Due to the fact that Ce^{3+} 5d and Mn^{2+} 3d energy levels are easily affected by its crystal field environment, herein, we further design a set of $Y_2SrAl_4SiO_{12}$: Ce^{3+} and $Y_2SrAl_4SiO_{12}$: Ce^{3+}, Mn^{2+} phosphors, and investigate the evolution of YAG microstructure and modulate its luminescence characteristics to obtain the more suitable yellow-red emission by energy transfer from Ce^{3+} to Mn^{2+} for White-Light-Emitting Diodes.

2. Experimental

$Y_{2-x}SrAl_4SiO_{12}$: $x$$Ce^{3+}$($x$=0, 0.04, 0.05, 0.06), $Y_{1.95}Sr_{1-y}Al_4SiO_{12}$: 0.05$Ce^{3+}$, $y$$Mn^{2+}$($y$=0.1-0.6) and $Y_{(1.95+z)}Sr_{(0.7-z)}Al_4Si_{12}$: 0.05$Ce^{3+}$, 0.3$Mn^{2+}$ (z=0.02, 0.06, 0.1) a series of samples were synthesized by the high-temperature solid-state reaction, using the raw materials of Y_2O_3 (99.99 %,Aladdin), $SrCO_3$ (99.95 %, Aladdin), Al_2O_3 (99.99 %, Aladdin), SiO_2 (99.99 %, Aladdin), CeO_2 (99.99 %, Aladdin), $MnCO_3$ (99.95 %, Aladdin). The raw materials were weighed in stoichiometric proportions, then mixed with an appropriate amount of ethanol (95%) using an agate mortar and pestle and thoroughly ground. After drying, the mixture was transferred to an alumina oxide crucible and then sintered in a tube furnace by heating to 1450 °C for 10 h, followed by furnace-cooling to room temperature. Finally, the sintered samples were completely ground into powders for characterization of XRD and photoluminescence properties. The crystal structure of the sintered samples was analyzed by an X-ray diffractometer (XRD, Rigaku, Ultima IV, Japan) with Cu-Ka radiation operated at 40 kV and 30 mA. The scanning rate was 8° min^{-1}, with a 2θ range from 20° to 80°. The

electronic structure of YAG and YSAS were analyzed by employing the density functional theory (DFT) using the GASTEP code. The photoluminescence (PL) and photoluminescence excitation (PLE) spectra were measured by a Spectro-fluorometer system (Fluorlog-3, HORIBA JOBIN YVON, France) equipped with a 450 W Xe-lamp. The fluorescence decay curve of the sample was determined with FLS-920T (Edinburg, UK). The luminescence properties under different temperature were measured by a standard phosphor thermal quenching analysis system (EX-1000, Hangzhou Ever fine co. LTD). The spectrum and performance test of w-LEDs devices are measured by LED light, color and electricity comprehensive testing instrument (HP9000, Hangzhou Hongpu Optoelectronics Technology Co., LTD).

3. Results and discussion

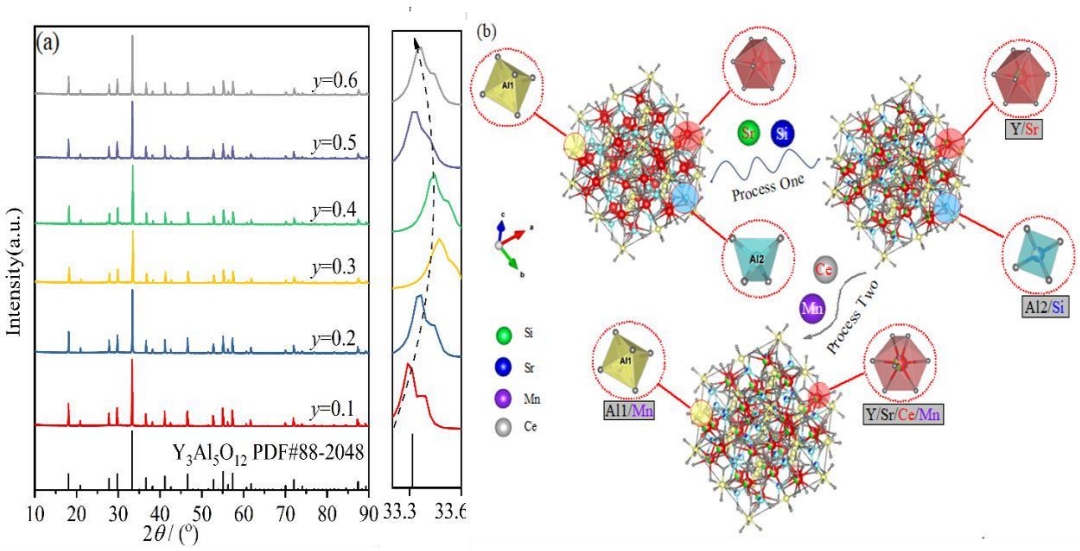

Fig. 1. XRD patterns of (a) YSAS: 0.05Ce^{3+}, $y$$Mn^{2+}$($y$=0.1-0.6) phosphors; (b) alternative schematic of YSAS crystal structure

Fig. S2 shows that the purity phase is verified by powder XRD for the samples of YSAS. All diffraction peaks are sharp and intense, and match well with the standard PDF card No.88-2048 of $Y_3Al_5O_{12}$, belonging to the cubic crystal system, *Ia3d* space group [16,17]. Herein, Sr^{2+} replaces Y^{3+} dodecahedral lattice sites, while Si^{4+} replaces $Al2^{3+}$ tetrahedral lattice sites to maintain charge balance. For YSAS: xCe^{3+} (x=0.04-0.06) phosphor, the XRD patterns are shown in Fig. S2. Since the ionic radius (in Table 1) and valence state of Ce^{3+} (CN=8) is similar to that of Y^{3+} (CN=8), Ce^{3+} is more inclined to replace Y^{3+} lattice sites to form Ce-O_8 dodecahedrons. The following spectroscopic study found that the optimal Ce^{3+} doping concentration was 0.05mol, so we carried out the Mn^{2+} co-doping study on the basis of YSAS: 0.05Ce^{3+}, and the XRD patterns of the YSAS: 0.05Ce^{3+}, yMn^{2+} (y=0-0.6) phosphors are shown in Fig. 1(a). No secondary phases composed of Ce^{3+} or Mn^{2+} were detected in any of the samples, which indicated that both Ce^{3+} and Mn^{2+} ions were completely dissolved into the lattice of YSAS matrix. The magnified profile of XRD diffraction pattern at 2θ angles from 33.2^o to 33.4^{o}s was drawn in right part of Fig. 1(a). Among them, the main peak (420) moves to high angle first and then to low angle, indicating that the site occupancy of Mn^{2+} in the matrix will change with the increase of Mn^{2+} doping concentration [18]. In previous studies [19,20], Mn^{2+} can be combined with six oxygen atoms to form an octahedron, and it can also be combined with eight oxygen atoms to form a dodecahedron. Therefore, according to the shift of the main diffraction peaks of XRD and previous studies, a conclusion can be drawn: when the Mn^{2+} doping concentration is lower than 0.3mol, Mn^{2+} mainly replaces Sr^{2+} (CN=8) with larger

ionic radius and combines with eight oxygen atoms to form Mn-O_8 octahedron, causing the main diffraction peaks to shift to higher angles; when the doping concentration of Mn^{2+} is higher than 0.3mol, Mn^{2+} begins to mainly replace Al^{3+} (CN=6, R=0.535 Å) with smaller ionic radius and combine with six oxygen atoms to form a Mn-O_6 octahedron, causing the main diffraction peak to shift to lower angles. Fig. 1(b) shows a schematic diagram of the incorporation of Sr-Si (Process One) as well as Ce-Mn (Process Two) units into the YAG structure. Among them, Ce^{3+} enters dodecahedral structure, Mn^{2+} not only enters dodecahedral structure, but also occupies octahedral structure.

Table 1 Partial octacoordinate ion radius information

ion	CN=8 (Å)
Y^{3+}	1.019 [14]
Ce^{3+}	1.143 [15]
Sr^{2+}	1.26 [14]
Mn^{2+}	0.96 [21]

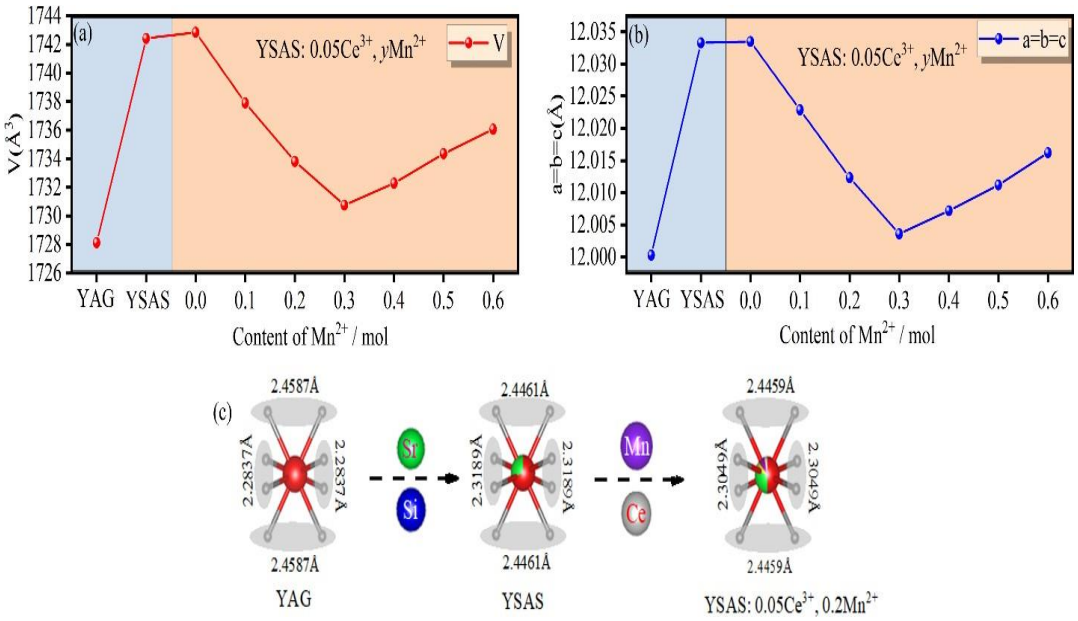

Fig. 2. (a) unit cell volume and (b) lattice parameters as a function of Mn^{2+} concentration; (c) dodecahedral bond lengths for some samples

In order to further study the structure of the samples, Rietveld structure refinement was performed on the YAG, YASA, and YASA: $0.05Ce^{3+}$, yMn^{2+} (y=0-0.6) series of samples, which are shown in Fig. S3. The refined data, lattice parameters, and unit cell volume obtained by refinement are shown in Table S1, and the bond length information is shown in Table S2. The changing trends of unit cell volume and lattice parameters are shown in Fig. 2(a) and (b), respectively. Among them, the changing trends of the YAG and YSAS matrix are shown with a light blue background. Due to the substitution of Y^{3+} (CN=8) for the large ionic radius Sr^{2+} (CN=8), the lattice parameter of the YSAS (a=b=c=12.03328 Å，V=1742.416 Å^3) matrix studied in this paper is larger than that of YAG (a=b=c=12.0003 Å, V=1728.13 Å^3) reported by Dobrzycki [22] et al. For YASA: $0.05Ce^{3+}$, yMn^{2+} (y=0-0.6) phosphors, the

corresponding background in Fig. 2(a), (b) are pale pink. The unit cell volume and lattice parameters first increased and then decreased with the increase of Mn^{2+} doping concentration, which was consistent with the shifting order of the main diffraction peaks. The changes in unit cell volume and lattice parameters indicate that Mn^{2+} was successfully incorporated into the lattice. Fig. 2(c) shows the bond lengths for dodecahedral refinement of YAG and doped Sr-Si and Ce-Mn units. Among them, the dodecahedral bond length of YAG is 2.4587 Å and 2.2837 Å, respectively, and the bond length difference is 0.175 Å. The dodecahedral bond length obtained by Sr-Si substitution is 2.4461 Å and 2.3189 Å, respectively, with a difference of 0.127 Å. The dodecahedral bond length (YSAS: $0.05Ce^{3+}$, $0.2Mn^{2+}$) obtained by Ce-Mn doping is 2.4459 Å and 2.3049 Å, respectively, with a difference of 0.141 Å. A larger difference usually means a more distorted polyhedron, otherwise a more perfect symmetry [23]. The substitution of Sr-Si reduces the bond length difference of the dodecahedron from 0.175 Å to 0.127 Å, indicating that the substitution of the Sr-Si unit makes the dodecahedron in the garnet structure have stronger symmetry and the structure is more rigid. In general, a more rigid structure has a positive effect on improving the luminescent properties. Doping Ce-Mn unit increases the difference of dodecahedron, but it is still smaller than that of YAG matrix, which means that the symmetry is still stronger than that of YAG matrix. More detailed bond lengths are shown in Table S2 and the average bond length of Y-O decreases from 2.3918 Å to 2.3587 Å with increasing Mn^{2+} concentration, which is due to the substitution of the smaller ionic radius Mn^{2+} for the larger ionic radius Sr^{2+}. Further observing the change of Al_1-O

bond length, when the concentration of Mn^{2+} is in the range of 0.1-0.3 mol, the increase of Al_1-O bond length is small (1.9294 Å to 1.9315 Å). However, when the doping concentration of Mn^{2+} exceeds 0.3 mol, the Al_1-O bond length changes greatly (1.9315 Å to 1.9493 Å), indicating that the higher of the Mn^{2+} concentration, the more obvious of the effect on the Al_1-O_6 octahedron.

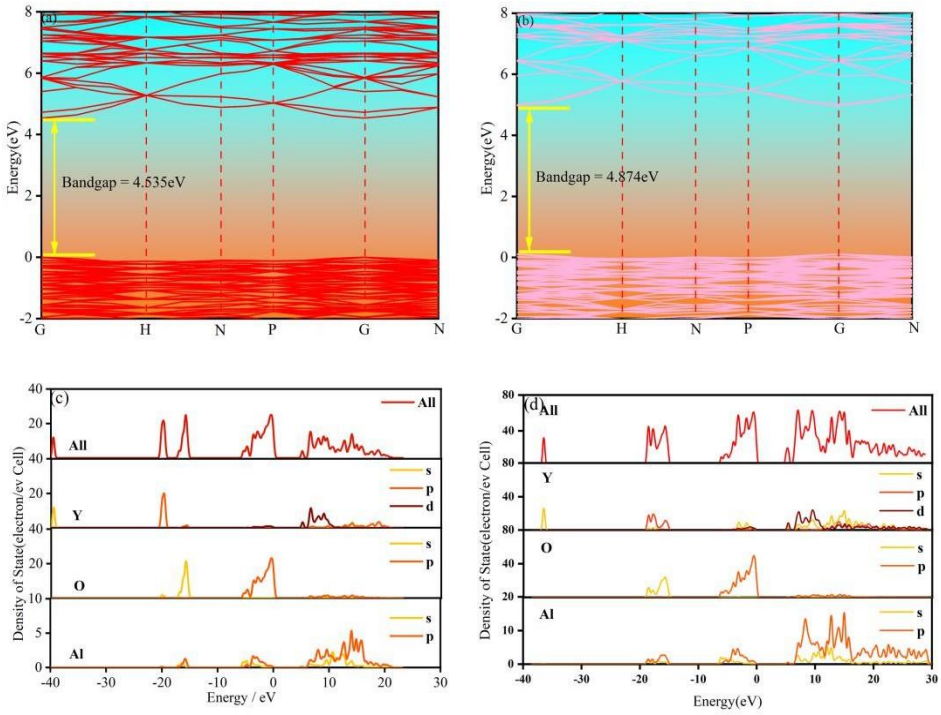

Fig. 3 DFT calculation of (a) YAG and (b) YSAS matrix band gap structure; Total DOS and PDOS of (c) YAG and (d) YSAS

Band structure is an important basis for analyzing optical properties. Fig. 3(a) and (b) are the band gap structure map obtained by DFT calculation. It can be seen that the band gap of pure YAG structure is 4.535 *e*V, and that of YSAS structure is 4.874 *e*V, and the doping of Sr-Si slightly increases the band gap of YAG. Whether it is a YAG structure or a YSAS structure, the bottom of the conduction band and the top of the

valence band are located at the *G* point, which belongs to the direct band gap structure. The electron distribution at the top of the valence band and the bottom of the conduction band has a great influence on the luminescence of the substance. Fig. 3(c) and (d) present the total density of states (DOS) and partial density of states (PDOS) of YAG and YSAS. From the density of states diagram, it can be seen that the top of the valence band of YAG is mainly composed of the O 2s states, and the bottom of the conduction band is mainly composed of the Y 4d states, Al 3s and 3p states. In the YSAS structure, the top of the valence band is mainly composed of the O 2s states, Al 3s states, Sr 5s states and the Si 3p states, and the bottom of the conduction band is mainly composed of the Y 4d stats, Sr 3d states, and the 2p and 3s states of O. These results suggest that the intrinsic absorption of YSAS mainly originates from the charge transfer from the Al 3s states to the O 2p state.

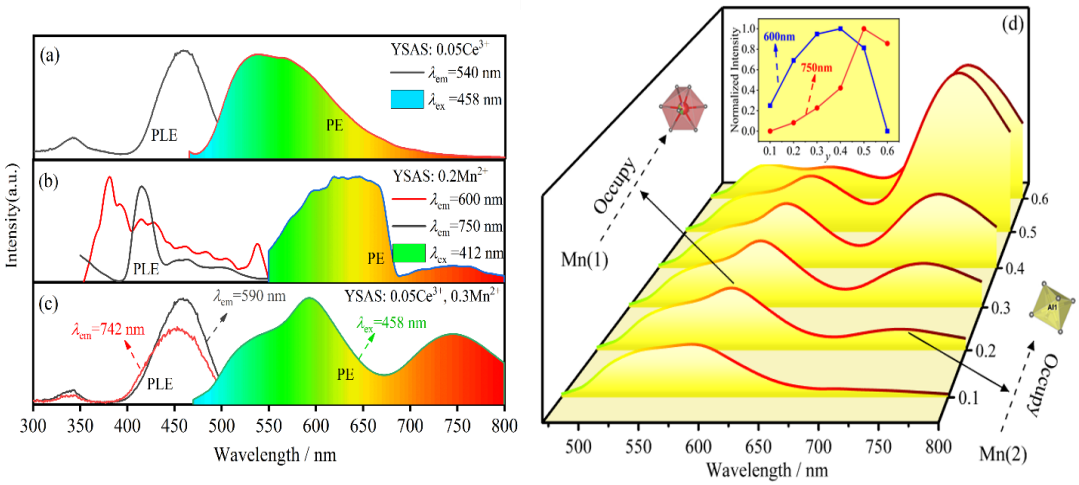

Fig. 4. (a) YSAS: 0.05Ce^{3+}; (b) YSAS: 0.2Mn^{2+}; (c) YSAS: 0.05Ce^{3+}, 0.3Mn^{2+} excitation and emission spectra; (d) normalized emission spectra of YSAS: 0.05Ce^{3+}, *y*Mn^{2+} (*y*=0.1-0.6) phosphors at 540 nm (λ_{ex} = 458 nm)

Under excitation at 365 nm, the optimal Ce^{3+} doping concentration of YSAS: $x$$Ce^{3+}$ is 0.05 mol, which is shown in Fig. S4. An attempt was made to increase the red component of the spectrum by co-doping Mn^{2+} on top of the optimal Ce^{3+} doping concentration. Fig. 4(a) shows the excitation and emission spectra of single-doped Ce^{3+}. Under excitation at 458 nm, YSAS: 0.05Ce^{3+} shows a broadband emission from 450 nm to 750 nm, with the strongest emission peak at 540 nm and a shoulder at 560 nm, which are attributed to the 5d-4f transition of Ce^{3+} ions. At the same time, under the detection of the strongest emission peak at 540 nm, the excitation spectrum of YSAS: 0.05Ce^{3+} phosphor shows the ultraviolet absorption band at 300-380 nm, and the blue absorption band at 400-550 nm, which can be efficiently excited by the blue InGaN LED chips. Fig. 4(b) shows the excitation and emission spectra of YSAS: 0.2Mn^{2+}. It can be seen that the single-doped Mn^{2+} sample exhibits two distinct emission bands under excitation at 412 nm, which can be attributed to the fact that Mn^{2+} occupies two luminescent sites in the YSAS matrix, and the emission peak originates from the $^4T_1(4G)$-$^6A_1(6S)$ transition of Mn^{2+}. The phenomenon exhibited by the spectra also supports the previous conclusion that Mn^{2+} will replace the dodecahedral and octahedral sites in the YSAS matrix. Under the detection of 600 nm, the sample exhibits a broadband excitation from 350 nm to 550 nm, and the excitation peaks are located at 375 nm, 412 nm, 455 nm, and 525 nm, respectively, originating from the transition of Mn^{2+} from $^6A_1$ to $^4T_2(4D)$, $^4A_1$ (4G), $^4E(4G)$, and $^4T_2(4G)$. To demonstrate that Mn^{2+} occupies two distinct luminescent sites, the excitation spectra at 600 nm and 750 nm were examined, respectively. There are two distinct excitation

spectra, demonstrating that Mn^{2+} occupies two distinct luminescent sites [24]. The emission peak of Mn^{2+} has a certain relationship with the coordination environment, which can be calculated by the equation (1) reported by Van Uitert [25,26]：

$$E(cm^{-1}) = Q \times [1 - (\frac{V}{4})^{\frac{1}{V}} \times 10^{\frac{-(nE_a r)}{80}}] \quad (1)$$

Where E is the emission site of Mn^{2+}; Q is the edge of the lower energy position of the free ion state; V is the valence state of Mn^{2+} ion (V=2); n is the coordination number of the site occupied by the dopant ion; E_a is the electron affinity of the atom forming the anion; r is the radius of the cation substituted by the activator. Since the ionic radius and coordination number of Sr^{2+} (CN=8, R=1.26 Å) are larger than those of Al^{3+} (CN=6, R=0.535 Å). Therefore, the 600 nm emission peak position corresponds to the Mn^{2+} occupying the dodecahedron Sr^{2+} site to form the Mn(1) luminescence center, and the 750 nm emission peak position corresponds to the Mn^{2+} occupying the octahedral Al^{3+} site to form the Mn(2) luminescence center. Fig. S5(a) shows the emission spectrum of Ce^{3+} and the excitation spectrum of Mn^{2+}, and there is overlap between the spectra, indicating the possibility of energy transfer from Ce^{3+} to Mn^{2+}. Fig. 4(c) shows the excitation and emission spectra of YSAS: 0.05Ce^{3+}, 0.3Mn^{2+} phosphors, and the sample exhibits a broadband emission in the range of 470-800 nm, indicating that the doping of Mn^{2+} expands the red emission band of the YSAS: Ce^{3+} phosphor. In order to analyze the composition of the emission spectra, Gaussian deconvolution was performed on the emission spectra of the YSAS: 0.05Ce^{3+}, 0.3Mn^{2+} samples under excitation at 458 nm. As shown in Fig. S5(b), four Gaussian curve peaks can be decomposed, and the center points at 2.39 *e*V (518 nm),

2.28 *e*V (543 nm), 2.10 *e*V (590 nm) and 1.67 *e*V (742 nm), respectively. Among them, the Gaussian peaks at 2.39 (518 nm) and 2.28 *e*V (543 nm) are due to the $^2D_{3/2}\rightarrow{}^2F_{5/2}$ and $^2D_{3/2}\rightarrow{}^2F_{7/2}$ transitions of Ce^{3+}, and the Gaussian peaks at 2.10 (590 nm) and 1.67*e*V (742 nm) are due to the two luminescent sites occupied by Mn^{2+}.

The normalized emission spectra of YSAS: $0.05Ce^{3+}$, yMn^{2+} (y = 0.1-0.6) phosphors at 540 nm under excitation at 458 nm are shown in Fig. 4(d), and the inset shows the intensity variation of the two Mn^{2+} emission sites. All samples exhibited not only Ce^{3+} emission at 540 nm, but also Mn^{2+} emission at 600 nm and 750 nm. It can be seen from the inset that the luminescence intensities at both Mn(1) and Mn(2) first increase and then decrease with increasing Mn^{2+} doping concentration. Among them, the luminescence intensity of Mn(1) reaches the strongest at x=0.4, and the luminescence intensity of Mn(2) reaches the maximum at x=0.5, and then decreases due to concentration quenching. It is worth noting that the luminescence intensity at Mn(2) has been increasing relative to that at Mn(1). When the doping concentration is less than 0.3 mol, the luminescence intensity at Mn(1) is greater than that at Mn(2), and when the doping concentration continues to increase, the luminescence intensity at Mn(2) will be stronger. There may be two reasons for the continuous enhancement of the luminescent sites at Mn(2). One reason is that according to the shift of the XRD diffraction peak and the change of the bond length, Mn^{2+} will preferentially occupy more dodecahedrons in the host. Therefore, Ce^{3+} will transfer more energy to the Mn(1) dodecahedron than to the Mn(2) octahedron. Although there is also a small amount of Mn^{2+} occupying the octahedral structure, the dodecahedron is dominant, so

the luminescence intensity at 600 nm is initially stronger than at 750 nm. However, as the doping concentration of Mn^{2+} keeps increasing, the luminescence sites of Mn(1) reach concentration quenching, and Ce^{3+} transfers more energy to Mn(2), resulting in a stronger luminescence intensity of Mn(2). Another reason is that in the YSAS: $0.05Ce^{3+}$ phosphor, since the ionic radius (Table 1) of Ce^{3+} (CN=8) is similar to that of Y^{3+} (CN=8), part of Ce^{3+} may non-equivalently replace Sr^{2+} instead of Y^{3+}, resulting in defects in the crystal structure and the substitution of divalent Mn^{2+} for trivalent Al^{3+} will make up for this defect, which will increase the number of Mn(2), resulting in the continuous enhancement of the luminescence intensity at Mn(2).

In order to prove the reliability of the second point of view, we design a set of experiments to make up for the defect caused by the replacement of Sr^{2+} by Ce^{3+} and by non-equivalent substitution of Sr^{2+} with Y^{3+}, which is proved by the following changes in the spectrum.

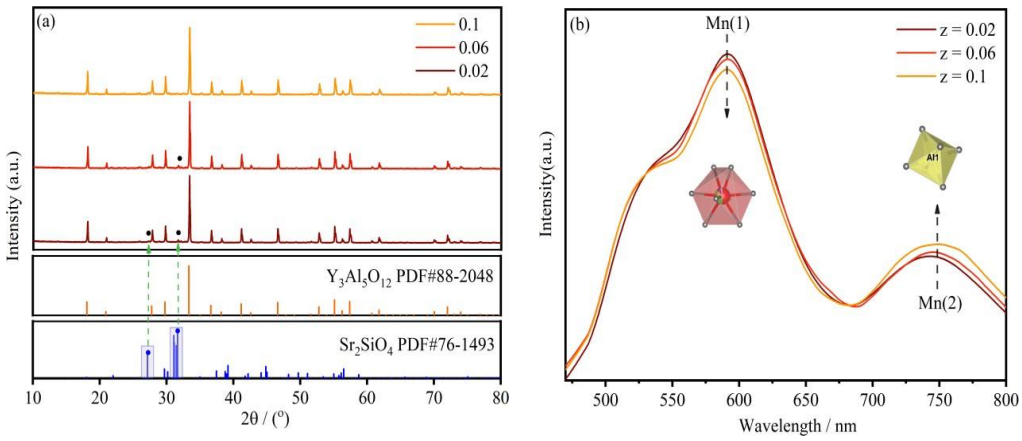

Fig. 5. (a) XRD patterns and (b) emission spectra of $Y_{(1.95+z)}Sr_{(0.7-z)}Al_4Si_{12}$: $0.05Ce^{3+}$, $0.3Mn^{2+}$ (z=0.02, 0.06, 0.1) phosphors

The XRD characterizations of different concentrations of Y^{3+} non-equivalently

substituted Sr^{2+} are shown in Fig. 5(a), when a smaller concentration of Y^{3+} is used instead of Sr^{2+}, the Sr_2SiO_4 second phase is generated. To determine the content of the second term, Rietveld dual-phase structure refinement was performed on the $Y_{(1.95+z)}Sr_{(0.7-z)}Al_4Si_{12}$: $0.05Ce^{3+}$, $0.3Mn^{2+}$ (z=0.02) sample, as shown in Fig. S6. Refinement refinement parameters R_p=9.48%, R_{wp}=8.12%, and the content of the second Sr_2SiO_4 obtained by refining is only 1.65%, which is extremely low. Besides, according to Wang [27] et al., the emission spectrum of Sr_2SiO_4: Ce^{3+} covers the range of 350 nm to 450 nm, which does not overlap with the emission spectrum range of 500-800 nm in this paper. Therefore, it can be considered that there is no emitting composition of Sr_2SiO_4: Ce^{3+} in the emission spectrum of this paper. Fig. 5(b) shows the emission spectra of different concentrations of Y^{3+} substituted for Sr^{2+}. With the unequal substitution of Sr^{2+} by Y^{3+}, the luminescence intensity of the Mn(1) luminescent site gradually decreases, while the luminescence intensity of the Mn(2) luminescent site gradually increases. This is due to the partial replacement of Sr^{2+} by Ce^{3+} leading to some defects inside YSAS: $0.05Ce^{3+}$, and the replacement of Al^{3+} by Mn^{2+} will make up for this defect, making more Mn^{2+} replace Al^{3+} and enhancing the luminescence intensity at Mn(2). This proves the reliability of the second point above.

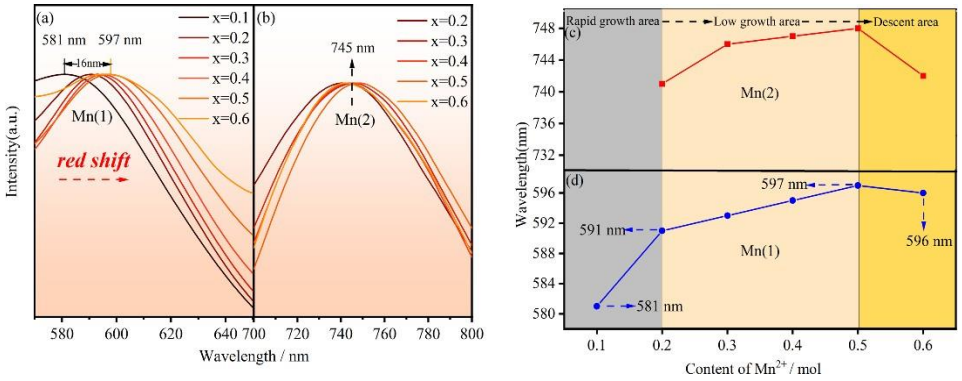

Fig. 6. (a) and (b) are schematic diagrams of the normalized peak position shift of YSAS: 0.05Ce^{3+}, $y$$Mn^{2+}$ (y=0.1-0.6) phosphors, respectively; (c) and (d) represent the peak position changes of different Mn^{2+} luminescent sites, respectively

The positions of the two normalized Mn^{2+} emission peaks are shown in Fig. 6(a) and (b), respectively. For Mn(1), the emission spectrum produces a red-shift of 16 nm, and the red-shift mainly occurs when the Mn^{2+} concentration is between 0.1-0.2 mol, while for Mn(2), the spectrum hardly changes. The concentration is divided into three regions according to the rate of red-shift, as shown in Fig. 6(c), (d). The concentration between 0.1-0.2 mol is called the rapid growth area, the concentration between 0.2-0.5 mol is called the low growth area, and the concentration between 0.5-0.6 mol is called the descent area. It can be seen that the red-shift of the emission peak originating from the Mn(1) luminescent site mainly occurs in the rapid growth area. The emission peaks at the luminescent sites of Mn(1) and Mn(2) in the low growth area both produce a slow red-shift. However, there is a blue-shift in both the descent area. For YSAS: 0.05Ce^{3+}, $y$$Mn^{2+}$($y$=0.1-0.6) phosphors, the luminescence spectrum

tuning phenomenon may mainly depend on the crystal field strength, and the crystal field splitting mainly describes the energy gap between the highest 5d energy level and the lowest 5d energy level. In general, the crystal field splitting can be calculated by (Dq) equation (2) [28,29]:

$$D_q = \frac{1}{6} Ze_2 \frac{r^4}{R^5} \tag{2}$$

Dq is the crystal field splitting energy; Z is the charge of the anion; e is the electron charge; r is the radius of the d wave function; R is the average bond length of the ions after substitution. In general, doping Mn^{2+} with a smaller ionic radius into the host lattice results in lattice shrinkage, which reduces the bond length between the activator and the anion, leading to larger crystal field splitting and red-shifted emission peak positions. However, this explanation may apply to the rapid and low growth area in Fig. 6(c) and (d), but it cannot explain the blue-shift in the descent area. In the YSAS host, the excellent structural rigidity of the garnet structure suppresses lattice shrinkage. Therefore, when some Mn^{2+} with a small ionic radius is doped into the host lattice, Mn^{2+} not only does not shorten the distance with the surrounding anions, but even becomes larger to maintain the excellent rigidity of the garnet structure [30]. The change in structural rigidity is related to symmetry and lattice distortion, which are calculated by the following formula (3) [31]:

$$D = \frac{1}{n} \sum_{i=1}^{n} \frac{|l_i - l_{av}|}{l_{av}} \tag{3}$$

Where D represents the lattice distortion, l_i is the distance from $Y^{3+}/Sr^{2+}/Mn^{2+}$ to the coordinating O atom, l_{av} is the average $Y^{3+}/Sr^{2+}/Mn^{2+}$-O^{2-} distance, and n is the coordination number. The calculated results are shown in Table 2. It can be found that

the distortion index of the MnO_8 polyhedron increases from D=16.70% to D=18.55% and then decreases to D=10.97% with the increase of Mn^{2+} concentration. The degree of distortion of the lattice shows a trend of increasing first and then decreasing, resulting in the symmetry of the dodecahedron decreasing first and then increasing. While the improvement of crystal field splitting results in a red-shift in the emission peak position, this red-shift is attenuated by the enhancement of the crystal structure stiffness and a blue-shift occurs.

Table 2 Distortion index of MO_8 polyhedron

x	*D*
0.0	0.016697
0.1	0.017264
0.2	0.018550
0.3	0.017312
0.4	0.016219
0.5	0.014696
0.6	0.010970

Furthermore, there are generally exchange interactions, radiation reabsorption, and electrical multipolar interactions during when energy transfer occurs, which are determined by the distance (R_c) between the sensitizer and the activator. R_c can be calculated from the following formula (4) [32,33]:

$$R_c \approx 2\left(\frac{3V}{4\pi x_c N}\right)^{\frac{1}{3}} \quad (4)$$

Where V represents the volume of the unit cell; X_c is the total concentration of sensitizer and activator, and N is the number of cations in the unit cell. For the studied samples, V=1736.799 Å^3, x_c=0.15~0.65, N=8, the critical distances in the samples are calculated to be 14.03~8.61 Å. When the distance is greater than 5 Å, the electric multilevel interaction is effective. What's more, the interaction type can be obtained from Dexter's formula (5) [34]:

$$\frac{I_{so}}{I_s} \propto C^{\frac{n}{3}} \quad (5)$$

Where I_{so} represents the initial emission intensity of Ce^{3+}; I_s represents the Ce^{3+} emission intensity of Ce^{3+}/Mn^{2+} co-doped phosphors; C represents the total concentration of Ce^{3+} and Mn^{2+} ions; n is a constant. When n=6, 8 and 10, they correspond to dipole-dipole, dipole-quadrupole, and quadrupole-quadrupole interactions, respectively. The curves fitted to I_{so}/I_s and $C_{n/3}$ are shown in Fig. S7. When n=6, the fit is best, indicating that the energy transfer from Ce^{3+} to Mn^{2+} is generated by dipole-dipole interaction.

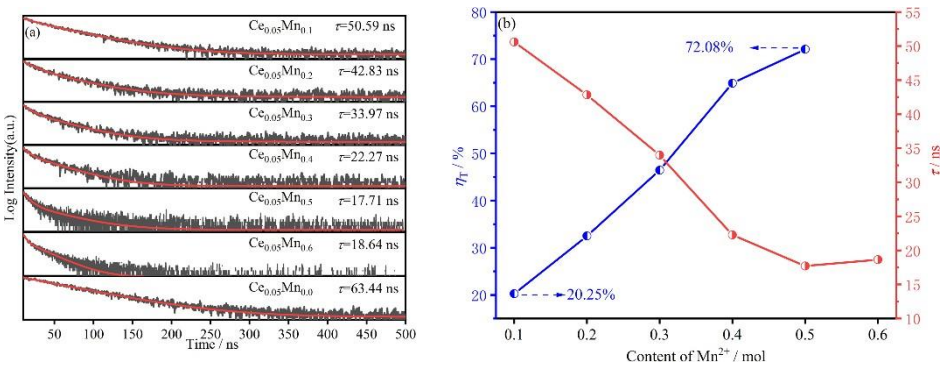

Fig. 7. (a) YSAS: 0.05Ce^{3+}, $y$$Mn^{2+}$($y$=0.0-0.6) series phosphors decay curve and lifetime; (b) Transfer efficiency from Ce^{3+} to Mn^{2+}

Under excitation at 458 nm and detection at 590 nm, the decay curves of YSAS: 0.05Ce^{3+}, $y$$Mn^{2+}$($y$=0.1-0.6) series phosphors at room temperature are shown in Fig. 7(a). The decay curve can be well fitted using the double exponential decay formula (6) [35]:

$$I(t) = A_1 \exp\left(\frac{-t}{\tau_1}\right) + A_2 \exp\left(\frac{-t}{\tau_2}\right) \tag{6}$$

Where I represent the luminous intensity of YSAS: 0.05Ce^{3+}, $y$$Mn^{2+}$ (y=0.1-0.6) at time t; A_1 and A_2 are fitting constants; τ_1 and τ_2 represent long-lived and short-lived, respectively. Then, the average fluorescence lifetime is calculated by the following formula (7) [36]:

$$\tau = \frac{A_1{\tau_1}^2 + A_2{\tau_2}^2}{A_1\tau_1 + A_2\tau_2} \tag{7}$$

The calculated lifetime is shown in Fig. 7(a). It can be observed that the lifetime of Ce^{3+} at 540 nm decreases with the increase of Mn^{2+} concentration, indicating that there is indeed energy transfer from Ce^{3+} to Mn^{2+}, and the energy transfer efficiency can be determined by the following formula (8) [37]:

$$\eta_T = 1\text{-}\frac{\tau}{\tau_0} \tag{8}$$

Where τ and τ_o represent the lifetimes of Ce^{3+} doped and undoped with Mn^{2+}. The obtained efficiency map is shown in Fig. 7(b). the transfer efficiency increases from 20.25% to 72.08%, and the energy transfer efficiency increases with the increase of Mn^{2+} doping concentration and reaches a maximum value at x=0.5.

The above analysis shows that Mn^{2+} occupies both dodecahedral and octahedral sites in the YASA structure, and Mn^{2+} has a preferential order for the occupation of these two sites. The bond energy method is used to evaluate the preferential occupation of the two light-emitting sites of Mn^{2+}, which can be calculated by the bond valence model (BVM), as shown in the following formula (9):

$$E_{M-O} = Jexp\left(\frac{d_o - d_{M-O}}{0.37}\right)\left(\frac{V_{\frac{Y}{Sr}}}{V_M}\right) \tag{9}$$

Where J is a constant equal to the standard atomization energy of a cationic simple oxide divided by the number of cations and the valence of the cations in the resulting oxide; d_o is a bond valence parameter; $d_{M\text{-}O}$ is the average bond length formed by cation occupancy; $V_{Y/Sr/Al}$ represents the valence state of the occupied cation; V_M represents the valence state of the cation. The bond energy of dodecahedron and octahedron occupied by Mn^{2+} can be determined by calculation, and the change of bond energy before and after Mn^{2+} doping can be compared by formula (10):

$$|\Delta E^{\frac{Y}{Sr}}_{M_n-O}| = |E_{M_n-O} - E_{\frac{Y}{Sr}}| \tag{10}$$

Among them, $E_{Mn\text{-}O}$ is the bond energy of the Mn-O bond in YSAS: $0.05Ce^{3+}$, $0.2Mn^{2+}$. $E_{Y/Sr/Al}$ is the bond energy of three different cationic Y/Sr/Al-O bonds in the YSAS matrix. The calculation results are shown in Table 3. The bond energy difference is Y/Sr-O>Al-O, and Mn^{2+} will preferentially occupy the sites with small changes in the bond energy difference, so Mn^{2+} will be more inclined to occupy the octahedral light-emitting site, and then the dodecahedron.

Table 3 YSAS key energy calculation

	$E_{Mn\text{-}O}$(kcal/mol)	$E_{Y/Sr/Al\text{-}O}$(kcal/mol)	$\Delta E_{M_n\text{-}O}^{Y/Sr/Al}$ (kcal/mo)
Y/Sr-O	34.55	51.51	16.96
Al1-O	60.30	57.09	3.21

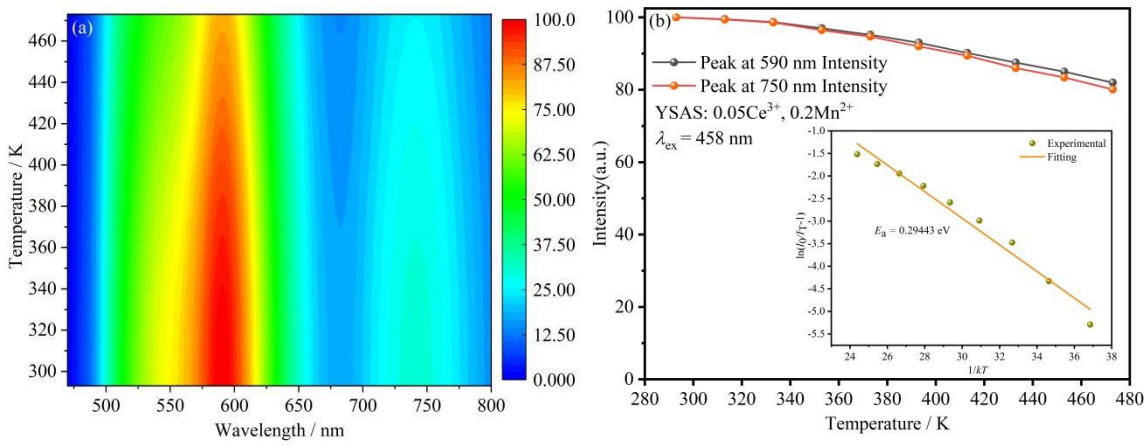

Fig. 8. (a) YSAS: 0.05Ce^{3+}, 0.2Mn^{2+} fluorescence intensity variation with temperature in the range of 293 K-473 K (λ_{ex}=458 nm); (b) 590 nm and 750 nm emission peak positions with temperature (λ_{ex}=458 nm), Inset shows calculated YSAS: 0.05Ce^{3+}, 0.2Mn^{2+} activation energy ΔE

Thermal stability is an important property to determine whether a phosphor can be commercialized and the thermal stability of YSAS: 0.05Ce^{3+}, 0.2Mn^{2+} phosphors is shown in Fig. 8(a). Under excitation at 458 nm, the overall luminescence intensity of the phosphors decreased gradually with the increase of temperature. Fig. 8(b) shows the trend of the intensities of the two luminescent spots occupied by Mn^{2+} as a function of temperature. It can be seen that the strength decreases slowly with increasing temperature. Among them, at 433 K, the luminescence intensity of the Mn(1) luminescence site at 590 nm is still 87.5% of that at room temperature, and the

luminescence intensity of the Mn(2) luminescence site at 750 nm remains 86%. At 473 K, they maintained 82% and 80.1% of room temperature, respectively, indicating excellent thermal stability. The excellent thermal stability of phosphors depends on their activation energy ΔE, which can be calculated by the Arrhenius formula (11) [38]:

$$I_T = \frac{I_0}{1+A\,exp(\frac{-\Delta E}{kT})} \tag{11}$$

Among them, I_T represents the luminescence intensity at T temperature, I_0 represents the initial luminescence intensity, A is a constant, K is the Boltzmann constant (8.617 × 10^{-5} eV K^{-1}), and ΔE represents the activation energy of thermal quenching. In the inset of Fig. 8(b), the relationship between $\ln(I_T/I_0 - 1)$ and $1/kT$ is plotted, with the negative of the slope being the desired activation energy ΔE, which is 0.29443 eV. Generally, the thermal stability of phosphors is positively correlated with the activation energy [39], so a larger activation energy leads to better thermal quenching performance of YSAS: 0.05Ce^{3+}, 0.2Mn^{2+} phosphors.

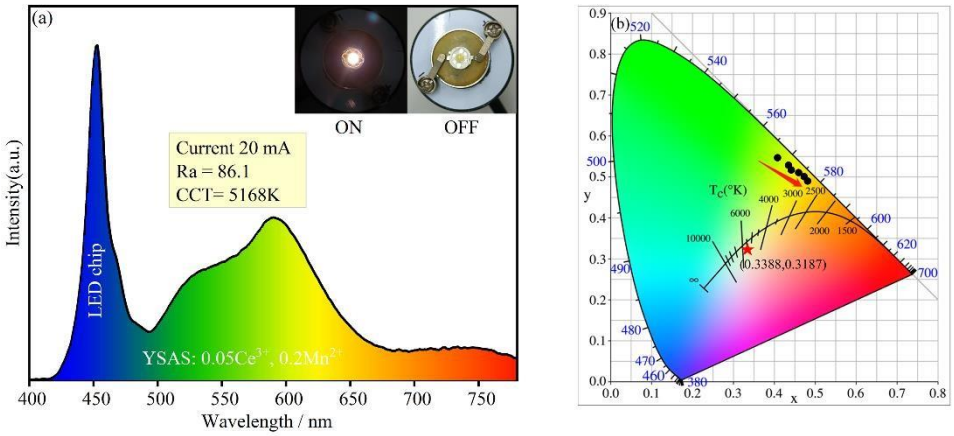

Fig. 9 (a) PL diagram of the w-LEDs device and (b) CIE coordinates of YSAS: 0.05Ce^{3+}, $y$$Mn^{2+}$($y$=0.0-0.6) phosphors ($\lambda_{ex}$=458 nm) and w-LEDs

To demonstrate the applicability, YSAS: $0.05Ce^{3+}$, $0.2Mn^{2+}$ phosphors were combined with blue light chips to produce white LEDs. Fig. 9 depicts the luminescence spectrum and related parameters of a w-LED driven by a 20mA current (a). Compared with the traditional commercial white light illumination, the white light LED produced by the phosphor has better color rendering ability (Ra=86.1) and lower color temperature (CCT=5186 K). The inset shows what the white LED looks like with and without current applied, which gives the device a dazzling white light. The CIE chromaticity coordinates displayed by the white light LED are shown in Fig. 9(b), the coordinates (0.3388, 0.3187) are located in the white light area, which has practical application value. With the increase of Mn^{2+} doping concentration, the color coordinates of phosphors under excitation at 458 nm red-shift from (0.4114, 0.5454) (YSAS: $0.05Ce^{3+}$) to (0.4781, 0.5166) (YSAS: $0.05Ce^{3+}$, $0.6Mn^{2+}$). The color of the sample changed from yellow-green to yellow, and then turned to orange-yellow, indicating that YSAS: $0.05Ce^{3+}$ can achieve tuning spectrum by doping Mn^{2+}.

4. Conclusion

YSAS: xCe^{3+}(x=0.04-0.06) and YSAS: $0.05Ce^{3+}$, yMn^{2+}(y=0.0-0.6) series phosphors were successfully synthesized by high temperature solid-phase method. The selective occupation of Mn^{2+} was preliminarily judged and verified by XRD and refinement. Mn^{2+} occupied the point of Sr^{2+} at low concentration to form a dodecahedral ligand, while occupied the point of Al^{3+} at high concentration to form an octahedral ligand. The emission peak corresponding to each luminous center was

determined by equation. The emission peak at 600nm was formed by MnO_8, and the emission peak at 750 mm was formed by MnO_6.Due to the enhancement of the crystal structure symmetry and structural rigidity caused by substitution of Sr-Si, the emission peak position of Mn(1) luminescent center at 585nm occurs the blue-shift. Because the non-equivalent substitution of Sr^{2+} by Ce^{3+} results in the crystal structure defective, Mn^{2+} replacing Al^{3+} lattice sites compensate for the charge defects, thereby increasing the amount of Mn(2), resulting in the continuous enhancement of the luminescence intensity at Mn(2) luminescent site. The energy transfer mechanism and efficiency from Ce^{3+} to Mn^{2+} were verified and calculated by analyzing the fluorescence spectrum and fluorescence decay curve, and the highest transfer efficiency could reach 72.8%. For the thermal stability, the luminescence intensity of the Mn(1) luminescent site at 585nm remain at 87.5%, and Mn(2) luminescence site at 750 nm remains 86% of room temperature at 433 K. Finally, w-LEDs were fabricated in combination with blue light chips, and the performance was Ra=86.1, CCT=5186K.

Acknowledgements

This work was supported by the National Natural Science Foundation of China under grant number: 51672063, 52161145401 and the Guangdong Key Platform & Programs of the Education Department of Guangdong Province for funding under Grant No. 2021ZDZX1003

Declaration of competing interest

The authors declare that they have no known competing financial interests or personal relationships that could have appeared to influence the work reported in this paper.

References

[1] Aggarwal R L, Ripin D J, Ochoa J R, et al. Measurement of Thermo-Optic Properties of $Y_3Al_5O_{12}$, $Lu_3Al_5O_{12}$, $YAlO_3$, $LiYF_4$, $LiLuF_4$, BaY_2F_8, $KGd(WO_4)_2$, and $KY(WO_4)_2$ Laser Crystals in the 80-300 K Temperature Range. *J. Appl. Phys*, 2005, 98(10): 103514.

[2] Ananias D, Kostova M, Paz F, et al. Photoluminescent Layered Lanthanide Silicates. *J. Am. Chem. Soc*, 2004, 126(33): 10410-10417.

[3] George N C, Pell A J, Dantelle G, et al. Local Environments of Dilute Activator Ions in the Solid-State Lighting Phosphor $Y_{3-x}Ce_xAl_5O_{12}$. *Chem. Mater*, 2013, 25(20): 3979-3995.

[4] Li Z, Liu B, Zhang Y, et al. Deep Red and White Light Emission Generated by $SrLaGa_3O_7$: Bi^{3+}, $SrLaGa_3O_7$: Mn^{4+} and $SrLaGa_3O_7$: Bi^{3+}/Mn^{4+} Phosphors. *J. Alloys Compd*, 2022, 894: 162455.

[5] Zhang S, Gai S, Zhang X, et al. Enhanced Luminescence Properties of Li_2MgTiO_4: Mn^{4+}, Ge^{4+} Phosphor Via Single Cation Substitution for Indoor Plant Cultivation. *Ceram. Int*, 2022, 48(3): 3070-3080.

[6] Cui M, Wang J, Shang M, et al. Full Visible Light Emission in Eu^{2+}, Mn^{2+}-Doped

$Ca_9LiY_{0.667}(PO_4)_7$ Phosphors Based On Multiple Crystal Lattice Substitution and Energy Transfer for Warm White LEDs with High Colour- Rendering. *J. Mater. Chem. C*, 2019, 7(12): 3644-3655.

[7] Huang X, Liang J, Rtimi S, et al. Ultra-High Color Rendering Warm-White Light-Emitting Diodes Based On an Efficient Green-Emitting Garnet Phosphor for Solid-State Lighting. *Chem. Eng. J*, 2021, 405: 126950.

[8] Wang S, Devakumar B, Sun Q, et al. Highly Efficient near-UV-excitable $Ca_2YHf_2Al_3O_{12}$: Ce^{3+}, Tb^{3+} Green-Emitting Garnet Phosphors with Potential Application in High Color Rendering Warm-White LEDs. *J. Mater. Chem. C*, 2020, 8(13): 4408-4420.

[9] Sun X, He Z, Gu X. Synthesis, Deep Red Emission and Warm WLED Applications of K_2SiF_6: Mn^{4+} Phosphors. *J. Photochem. Photobiol., A*, 2018, 350: 69-74.

[10]Liu C, Zhang B, Hao L, et al. Synthesis and Photoluminescent Properties of $Sr_2Si_5N_8$: Eu^{2+} Red Phosphors for White Light-Emitting Diodes. *J. Rare Earths*, 2014, 32(8): 691-695.

[11]Ali A G, Dejene B F, Swart H C. The Influence of Oxygen Partial Pressure On Material Properties of Eu^{3+}-Doped Y_2O_2S Thin Film Deposited by Pulsed Laser Deposition. *Physica B*, 2016, 480: 174-180.

[12]Tong E, Song K, Deng Z, et al. Ionic occupation sites, luminescent spectra, energy transfer behaviors in $Y_3MgAl_3SiO_{12}$: Ce^{3+}, Mn^{2+} phosphors for warm white LED. *J. Lumin*, 2020, 217: 116787.

[13]Jia Y, Huang Y, Zheng Y, Guo N, et al. Color Point Tuning of $Y_3Al_5O_{12}$: Ce^{3+} Phosphor Via Mn^{2+}-Si^{4+} Incorporation for White Light Generation. *J. Mater. Chem*, 2012, 22(30): 15146-15152.

[14]Ji H, Wang L, Cho Y, et al. New $Y_2BaAl_4SiO_{12}$: Ce^{3+} Yellow Microcrystal-Glass Powder Phosphor with High Thermal Emission Stability. *J. Mater. Chem. C*, 2016, 4(41): 9872-9878.

[15]Meng Q, Li J, Zhu Q, et al. The Effects of Mg^{2+}/Si^{4+} Substitution On Crystal Structure, Local Coordination and Photoluminescence of $(Gd, Lu)_3Al_5O_{12}$: Ce Garnet Phosphor. *J. Alloys Compd*, 2019, 797: 477-485.

[16]Skruodiene M, Juodvalkyte R, Inkrataite G, et al. Sol-Gel Assisted Molten-Salt Synthesis of Novel Single Phase $Y_{3-2x}Ca_{2x}Ta_xAl_{5-x}O_{12}$: 1%Eu Garnet Structure Phosphors. *J. Alloys Compd*, 2022, 890: 161889.

[17]Jia J, Qiang Y, Xu J, et al. A Comparison Study On the Substitution of Y^{3+}-Al^{3+} by M^{2+}-Si^{4+}(M = Ba, Sr, Ca, Mg) in $Y_3Al_5O_{12}$: Ce^{3+} Phosphor. *J. Am. Ceram. Soc*, 2020, 103(9): 5111-5119.

[18]Yang C, Fan C, Hussain F, et al. Sn^{4+} Induced Bi^{3+} Multi-Lattice Selective Occupation and its Color-Tunable Emission of La_2MgZrO_6 : Bi^{3+}, Sn^{4+} Double Perovskite Phosphors. *J. Alloys Compd*, 2022, 902: 163724.

[19]Liu Y, Zhang X, Hao Z, et al. Tunable Full-Color-Emitting $Ca_3Sc_2Si_3O_{12}$: Ce^{3+}, Mn^{2+} Phosphor Via Charge Compensation and Energy Transfer. *Chem. Commun*, 2011, 47(38): 10677-10679.

[20]Wang Z, Li P, Liu J, et al. Using Multi-Site Substitution to Design Blue-Exciting

Phosphor $Mg_2Y_2Al_2Si_2O_{12}$: Mn^{2+} for Full-Spectrum Plant Growth LEDs. *J. Lumin*, 2021, 234: 117943.

[21]Zhang S, Li Y, Lv Y, et al. A full-color emitting phosphor $Ca_9Ce(PO_4)_7$: Mn^{2+}, Tb^{3+}: Efficient energy transfer, stable thermal stability and high quantum efficiency. *Chem. Eng. J*, 2017, 322: 314-327.

[22]Dobrzycki L, Bulska E, Pawlak D A, et al. Structure of YAG Crystals Doped/Substituted with Erbium and Ytterbium. *Inorg. Chem*, 2004, 43(24): 7656-7664.

[23]Bi Y, Yang H, Yun X, et al. Tailoring Narrow-Band Blue Emitting $Ca_7(Mg, Zn)_2P_6O_{24}$: Eu^{2+} Phosphate Phosphor Via Crystal Lattice Distortion for WLEDs. *Opt. Mater*, 2020, 107: 110094.

[24]Qian H, Fan C, Hussain F, et al. Energy Transfer Between Two Luminescent Centers and Photoluminescent Properties of $Ca_{4-y}La_6(AlO_4)_x(SiO_4)_{6-x}O_{1-x/2}$: yEu^{2+} Apatite Structure Phosphors. *J. Lumin*, 2021, 235: 117991.

[25]Yang J, He P, Xie Y, et al. A High Absorption Efficiency Blue-Emitting Phosphor $NaSrScSi_2O_7$: Eu^{2+} for near-UV-pumped White Light-Emitting Diodes. *J. Alloys Compd*, 2022, 903: 163815.

[26]Zhang B, Zhang X. Zhang D, et al. Ultra-wideband phosphor $Mg_2Gd_8(SiO_4)_6O_2$: Ce^{3+}, Mn^{2+}: Energy transfer and pressure-driven color tuning for potential applications in LEDs and pressure sensors. *Chem. Eng. J*, 2022, 427: 131897.

[27]Wang L, Li Y, Wang Z, et al. Resonant Energy Transfer and Near-Infrared Emission Enhanced by Tri-Doped Sr_2SiO_4: Ce^{3+}, Tb^{3+}, Yb^{3+} Phosphors for

Silicon Solar Cells. *J. Lumin*, 2018, 203: 121-126.

[28]Ding X, Zhu G, Geng W, et al. Novel Blue and Green Phosphors Obtained From $K_2ZrSi_3O_9$: Eu^{2+} Compounds with Different Charge Compensation Ions for LEDs Under near-UV Excitation. *J. Mater. Chem. C*, 2015, 3(26): 6676-6685.

[29]Shang M, Liang S, Qu N, et al. Influence of Anion/Cation Substitution ($Sr^{2+} \rightarrow Ba^{2+}$, $Al^{3+} \rightarrow Si^{4+}$, $N^{3-} \rightarrow O^{2-}$) On Phase Transformation and Luminescence Properties of $Ba_3Si_6O_{15}$: Eu^{2+} Phosphors. *Chem. Mater*, 2017, 29(4): 1813-1829.

[30]Zhang X, An Z, Dong R, et al. Properties and Application of Single Eu^{2+}-Activated Color Tuning Phosphors. *ACS Sustainable Chem. Eng*, 2019, 7(12): 10724-10733.

[31]Denault K A, Brgoch J, Gaultois M W, et al. Consequences of Optimal Bond Valence on Structural Rigidity and Improved Luminescence Properties in $Sr_xBa_{2-x}SiO_4$: Eu^{2+} Orthosilicate Phosphors. *Chem. Mater*, 2014, 26(7): 2275-2282.

[32]Yun X, Zhou J, Zhu Y, et al. A Potentially Multifunctional Double-Perovskite Sr_2ScTaO_6: Mn^{4+}, Eu^{3+} Phosphor for Optical Temperature Sensing and Indoor Plant Growth Lighting. *J. Lumin*, 2022, 244: 118724.

[33]Tang H, Zhang X, Cheng L, et al. Crystal Structure, Luminescence Properties and Thermal Stability of Lu^{3+} Ion-Substituted $BaY_2Si_3O_{10}$: Dy^{3+} Phosphors. *J. Alloys Compd*, 2022, 898: 162758.

[34]Zhang B, Ying S, Wang S, et al. Blue-Green-Yellow Color-Tunable Luminescence of Ce^{3+}-, Tb^{3+}-, and Mn^{2+}-Codoped $Sr_3YNa(PO_4)_3F$ Via Efficient Energy Transfer. *Inorg. Chem*, 2019, 58(7): 4500-4507.

[35]Zhu X, Ma X, Ali R N, et al. A Novel and Efficient Method for the Synthesis of Strong Fluorescence and Long Afterglow BPO_4 Phosphors. *Ceram. Int*, 2022, 48(6): 8209-8215.

[36]Qu M, Zhang X, Mi X, et al. Novel Color Tunable Garnet Phosphor of Tb^{3+} and Eu^{3+} Co-Doped $Ca_2YZr_2Al_3O_{12}$ with High Thermal Stability Via Energy Transfer. *J. Alloys Compd*, 2020, 828: 154398.

[37]Pasinski D, Sokolnicki J. Broadband Orange Phosphor by Energy Transfer Between Ce^{3+} and Mn^{2+} in $Ca_3Al_2Ge_3O_{12}$ Garnet Host. *J. Alloys Compd*, 2019, 786: 808-816.

[38]Huang S, Shang M, Peng K, et al. Garnet-Type Far-Red Emitting $Li_6CaLa_2Nb_2O_{12}$: Mn^{4+}, Bi^{3+} Phosphor for Full-Spectrum White LED. *J. Lumin*, 2022, 243: 118649.

[39]Zheng B, Zhang X, Zhang D, et al. Ultra-Wideband Phosphor $Mg_2Gd_8(SiO_4)_6O_2$: Ce^{3+}, Mn^{2+}: Energy Transfer and Pressure-Driven Color Tuning for Potential Applications in LEDs and Pressure Sensors. *Chem. Eng. J*, 2022, 427: 131897.